2023 IEEE International Conference on Robotics and Automation (ICRA 2023)
May 29 - June 2, 2023. London, UK

An Optimized Portable Cable-Driven Haptic Robot Enables Free Motion and Hard Contact

Changqi Zhang, Cui Wang, Qingkai Yang, and Mingming Zhang*, *Senior Member, IEEE*

Abstract— **Task-oriented training with haptic rendering can boost robot-aided motor learning to tasks with similar dynamics. Although multi-DOF robots better match the rendering of real task scenarios, single-DOF haptic robots show great potential for home use with enhanced task rendering performance. This study presents our attempts to optimize and develop a single-DOF cable-driven robot with appropriate workspace and force rendering capacity. The core technologies consist of two aspects: 1) a multi-objective optimization method was adopted to obtain optimal configuration of the haptic robot; and 2) a slider-crank-mechanism-based portable cable-driven robot was developed. Performance evaluation experiments demonstrated that 1) the robot has a workspace larger than 300 mm; 2) the robot can achieve 40 N force output and 40 N $\cdot$ mm^{-1} stiffness for hard contact; 3) the root mean square of the resistance during free motion is 0.93 N; 4) in the purely passive case (without motor compensation), the average resistance to back drive the motor is 2.5 N. These lead us to believe that the developed robot holds the promise to serve as a robotic rehabilitation training platform for home use on the neurological-impaired patients.**

I. Introduction

Numerous studies indicated the efficacy of robot-assisted task-specific training in neuro-rehabilitation [1-3]. Robotic devices that enable in-home use allow patients to receive professional training assistance in their own homes, thereby extending the training time and accelerating the recovery process. As haptic robots can provide precise sensorimotor feedback [4, 5], home-based task-oriented training with haptic rendering holds the promise to boost robot-aided motor and skill learning to tasks with similar dynamics [6].

According to the degrees of freedom (DOFs) of rendering tasks, haptic robots can be divided into single-DOF and multi-DOF robots. Multi-DOF robots provide motion in two or more dimensions that match the operational scenario of the real task better than single-DOF types. Numerous multi-DOF robots have been developed [7-9], most of which, however, have complex mechanical design that makes them difficult to be accurately controlled. Additionally, they are not portable enough for home use and are too expensive for most people.

In contrast, the single-DOF robot has advantages in portability and cost. Single-DOF robots, although the matching between the motion and the real task is not as good as that of the multi-DOF systems, are easier to achieve accurate control and high-fidelity task rendering. Further, a wide range of terminal linear motion can also realize the training of multiple muscle groups [10]. Therefore, it would be of great practical interest to develop portable, low-cost, and high-performance single-DOF (translational) haptic robots to perform task-oriented training [11]. However, the existing single-DOF robots generally use ballscrews, belts, pulleys, etc. [12-14]. This can lead to system friction and backlash and hence deteriorate haptic rendering performance.

It is noted that cable transmission has benefits of no backlash, low friction, low cost, and high efficiency [15]. Nevertheless, since cable can only pull but not push, cable transmission cannot transfer rotary motion of a single motor into linear reciprocating motion directly [16]. Specific mechanism needs to be designed for bidirectional force output, leading to a relatively large robot size to meet workspace requirements. Hence, demands of portability and workspace should be balanced. On top of that, an appropriate haptic robot should also be capable of rendering tasks of free motion and hard contact that generally represents the kinematic and kinetic properties of real daily tasks. Free motion needs the robot to have low inertia, while hard contact requires high force and stiffness output [17, 18]. This poses a major challenge to implement both free motion and hard contact from the view of robotic design and optimization. In general, multi-objective optimization is essential to guarantee both kinematic and kinetic performance of the robot.

This paper developed a haptic robot with optimized kinematic and kinetic configuration, consisting of robot optimization and design, robot development, and haptic rendering control. The contributions can be summarized as 1) the optimal robot configuration delivering suitable workspace, portability, and force rendering capacity was obtained via a multi-objective optimization; 2) a slider-crank-mechanism-based portable cable-driven robot was developed enabling free motion and hard contact; 3) extensive experiments were conducted to validate the performance of the developed robot.

II. Robot Optimization

To develop the robot system with an optimal configuration, the optimization process was designed as shown in Fig. 1. The

We acknowledge the funding supports from the National Natural Science Foundation of China (Grant No. 62273173), Shenzhen Key Laboratory of Smart Healthcare Engineering (Grant No. ZDSYS20200811144003009), the Research Foundation of Guangdong Province (Grant No. 2020ZDZX3001, Grant No. 2019ZT08Y191, and Grant No. 2022B1212010003). (*Corresponding author: Mingming Zhang*)

C. Zhang, C. Wang, Q. Yang, and M. Zhang are with Shenzhen Key Laboratory of Smart Healthcare Engineering, and also with Guangdong Provincial Key Laboratory of Advanced Biomaterials, the Department of Biomedical Engineering at Southern University of Science and Technology, Nanshan District, Shenzhen 518055, China (e-mail: 11930924@mail.sustech.edu.cn; wangc33@mail.sustech.edu.cn; yangqk@mail.sustech.edu.cn; zhangmm@sustech.edu.cn)

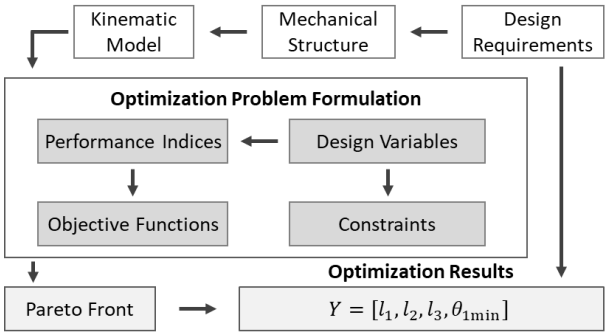

Fig. 1. Scheme of the optimization process.

detailed description is in the remainder of this section.

A. Design Requirements and Analysis

- Transmission system. Cable-driven mechanism should be adopted for a low gear ratio (denoted as γ). Determination of γ can refer to the research of multi-DOF robots, such as CASIA-ARM (20:1) [19], Delta-R (14:1) [20], and Delthaptic (16:1) [21]. This study chose a smaller γ value of 12:1.
- Force rendering capacity. Haptic rendering of hard contact requires the device to have sufficient stiffness and force output capacity. The work of [22] suggested that approximately 40 N of resistance would be substantial for patients with neurological injury. Therefore, the value of force output capacity was set as $f = 40$ N [3, 23].
- Workspace. A required minimal range of motion (ROM) exists in the joints of the upper limb for completing ADLs [24]. Referring to the work in [25], ROM of some general ADL tasks can be defined as 40 % of arm length for the upper-limb training purpose. Therefore, 300 mm was adopted as the workspace [26, 27].
- Portable design. To make the robot portable, the minimal robot size needs to be defined. For the developed robot, its maximal size appears in the length direction. Referring to the works in [22] and [28], the maximum length of the robot was set as 700 mm.

B. Geometric Descriptions

Considering the successful application of five-linkage mechanism in haptic robots [29], a slider-crank-mechanism-based single-DOF robot was designed as shown in Fig. 2 (a). This mechanism consists of a motor, a cable wheel, an active joint, a passive joint, two links, and a rail. The motor drives the wheel via the cable transmission (Fig. 2 (b)), and link 1 is actuated. Then link 2 transmits the motion to the handle.

Fig. 2 (c) illustrates the kinematic model, where the active joint is denoted as A and the passive joint as B, and C is the output endpoint. A plane-coordinate O-xy is located at the point of O. Let $X = (x, y)^{\mathrm{T}}$ be the coordinate of point C. According to the geometric relationship, we get

$$\begin{cases} x = l_1 \cos\theta_1 + l_2 \cos(\theta_1 + \theta_2) + l_3 \\ y = l_1 \sin\theta_1 + l_2 \sin(\theta_1 + \theta_2) \end{cases} \quad (1)$$

where $|AB|$=l_1, $|BC|$=l_2, $|OA| = l_3$, θ_1 and θ_2 are angles of the active joint and passive joint, respectively, θ_2 is determined by θ_1.

By solving (1), the solutions of inverse kinematics can then be obtained. To obtain the Jacobian matrix, differentiating (1) with respect to time, which yields

$$\dot{X} = J\dot{\theta} \quad (2)$$

where J is the Jacobian matrix, $\dot{X}$ is the linear velocity vector, and $\dot{\theta}$ is the angular velocity vector.

The robot workspace can be determined by (1). Due to mechanical limit, the input angle satisfies $\theta_1 \in [\theta_{1min}, \theta_{1max}]$. Then the range of motion of the endpoint can be obtained by

$$y_{min} < y < y_{max} \quad (3)$$

where y_{min} and y_{max} are the coordinates of endpoint C when the input angle θ_1 is set as θ_{1min} and θ_{1max}, respectively.

C. Optimization Problem Formulation

Based on the kinematic analysis, $Y = [l_1, l_2, l_3, \theta_{1min}]$ was selected as the vector of design variables. Range of θ_1 was constrained by the mechanical limit ($\theta_{1max} - \theta_{1min} = 135°$). To get a minimal robot size and meet the workspace requirements, the range of design variables was set as

$$\aleph = \begin{cases} \theta_{1min} \in [\alpha_1, \alpha_2] \\ l_1 \in [l_{1min}, l_{1max}] \\ l_2 \in [l_{2min}, l_{2max}] \\ l_3 \in [l_{3min}, l_{3max}] \end{cases} \quad (4)$$

where $\alpha_1 = -65°$, $\alpha_2 = -50°$, $l_{1min} = l_{2min} = 100\text{mm}$, $l_{1max} = l_{2max} = 300\text{mm}$, $l_{3min} = 0$, $l_{3max} = 100\text{mm}$.

Considering the kinematic relationships, several constraints were defined to meet the design requirements.

- For this non-Cartesian mechanism, different motor torques are needed to generate same output force. The calculated torques of all points (denoted as $\tau_k, k = 1,2,\dots,n$) should be within the motor capacity, i.e., $\tau_k < \tau_{max}$.
- Given a specified Y, the workspace can be determined by $y_{max} - y_{min}$, which should be larger than the defined workspace L_w. Meanwhile, for portability, the total length of the equipment L_r should be less than the maximum allowable length L_{max}.
- Link collisions between link 2 and wheel shaft might occur due to physical size of the link. Assuming that the distance is d_{min} when the link is tangent to the shaft, the distance d_{ls} between the link and shaft should be larger than d_{min}.
- Two kinds of singular configurations exist including inverse and direct kinematic singularities. Determinant of the Jacobian matrix was constrained by $\|J\| \neq 0$ or ∞.

A large workspace generally produces a large robot size that is incompatible with the portable design. Hence a compact size was selected as the optimization goal. L was defined as one of the performance evaluation indices.

$$L = l_1 + l_3 \quad (5)$$

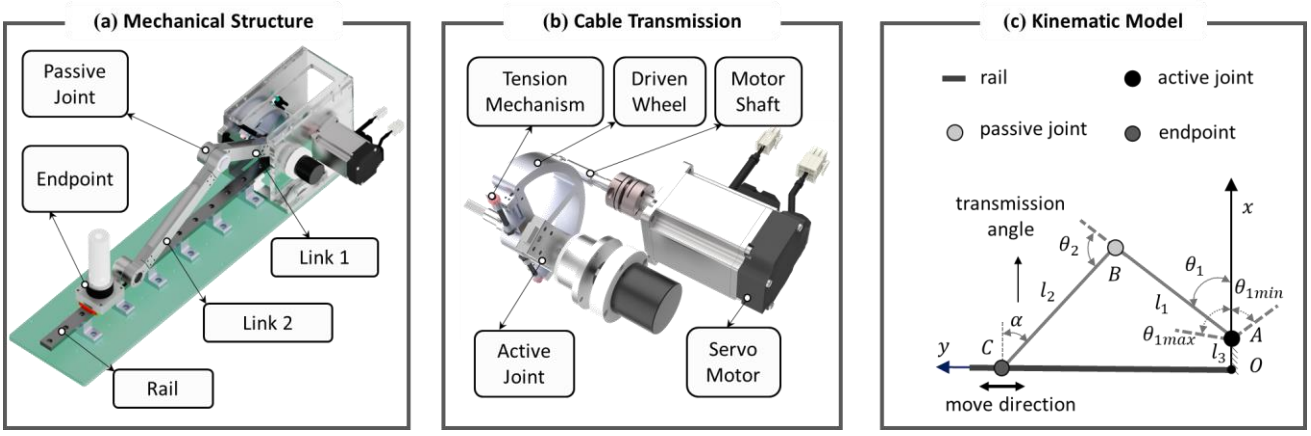

Fig. 2. (a) Mechanical structure of the single-DOF haptic robot. (b) Cable transmission mechanism with a low reduction ratio (12:1). (c) Kinematic model of the haptic robot.

The global conditioning index (denoted as κ_w) was defined by (6) to evaluate the accuracy index [30].

$$\kappa_w = \frac{1}{n}\sum_{i=1}^{n} 1/\kappa_i \ , 0 \le \kappa_w \le 1 \tag{6}$$

where n is the total number of discrete points in the workspace, and κ_i is the condition number of the ith point.

For the crank-slider mechanism, the force applied to the handle includes x-axis and y-axis components (denoted as F_x and F_y respectively). A lightweight robot needs a small value of F_x. In addition, F_x tends to increase the frictional force. Therefore, a minimized F_x is needed. Let F_{xmax} denote the maximum allowable F_x, so $F_x < F_{xmax}$ was defined. As shown in Fig. 2 (c), the transmission angle α can be calculated by $\arctan(F_y/F_x)$, where α is negatively correlated with F_x. To this end, the global transmission angle α_w, defined by (7), was selected as another optimization objective.

$$\alpha_w = \frac{1}{n}\sum_{i=1}^{n} 1/\alpha_i \ , 0 < \alpha_w < 90° \tag{7}$$

where n is the total number of discrete points, and α_i is the transmission angle of the ith point.

From the above analysis, the design can be considered as a multi-objective optimization problem to obtain a minimum L, a maximum κ_w, and a maximum α_w. Mathematically, formulation of the optimization problem can be stated as:

Finding the vector Y that

$$\min f(Y) = \min \begin{cases} f_1 = L \\ f_2 = -\kappa_w \\ f_3 = -\alpha_w \end{cases} \tag{8}$$

subject to

$$\begin{cases} Y \in \aleph, \tau_k < \tau_{max}, F_x < F_{xmax}, \|J_1\| \neq 0 \text{ or } \infty \\ d_{ls} > d_{min}, y_{max} - y_{min} > L_w, L_r < L_{max} \end{cases} \tag{9}$$

The range of the variables is set as $\tau_{max} = 15\ \mathrm{N \cdot m}$, $F_{xmax} = 100\ \mathrm{N}$, $L_w = 300\ \mathrm{mm}$, $L_{max} = 700\ \mathrm{mm}$, $d_{min} = 40\ \mathrm{mm}$.

D. Optimization Results

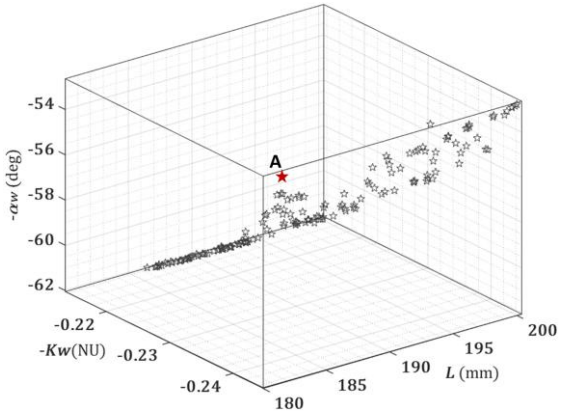

Fig. 3. Pareto front solutions for the multi-objective optimization problem.

For this nonlinear constraint optimization problem, the genetic algorithm (GA) was adopted. A GA-based multi-objective optimization toolbox (a variant of NSGA-II [31]) in MATLAB R2020b (MathWorks, Natick, MA, US) was used to optimize the three objectives (L, κ_w, and α_w), where the population size is 200, number of iteration is 200, crossover probability is 0.5, and the mutation function is the Adaptive Feasible (mutationadaptfeasible). Then Pareto front solutions were obtained shown in Fig. 3. Finally, the intermediate solution $A\,(0.18, -0.24, -53.4)$ was defined as the configuration of the haptic robot since it can make a good tradeoff among the three objectives. The corresponding vector of design variables is Y=[183, 234, 0, −50].

III. Robot Development

A. Prototype

Prototype of the haptic robot is shown in Fig. 4 (a). The robot is actuated by one AC servo motor (rated torque: 1.27 N · m, Panasonic, MSMF042L1U2M, Japan) with the driver (Panasonic, MBDLN25BE, Japan). A linear guide rail, fixed on the base, is connected to the handle. In human-robot interaction tasks, the participant can grasp and move the handle forward and backward. The total length of the robot is 650 mm which meets the design requirements.

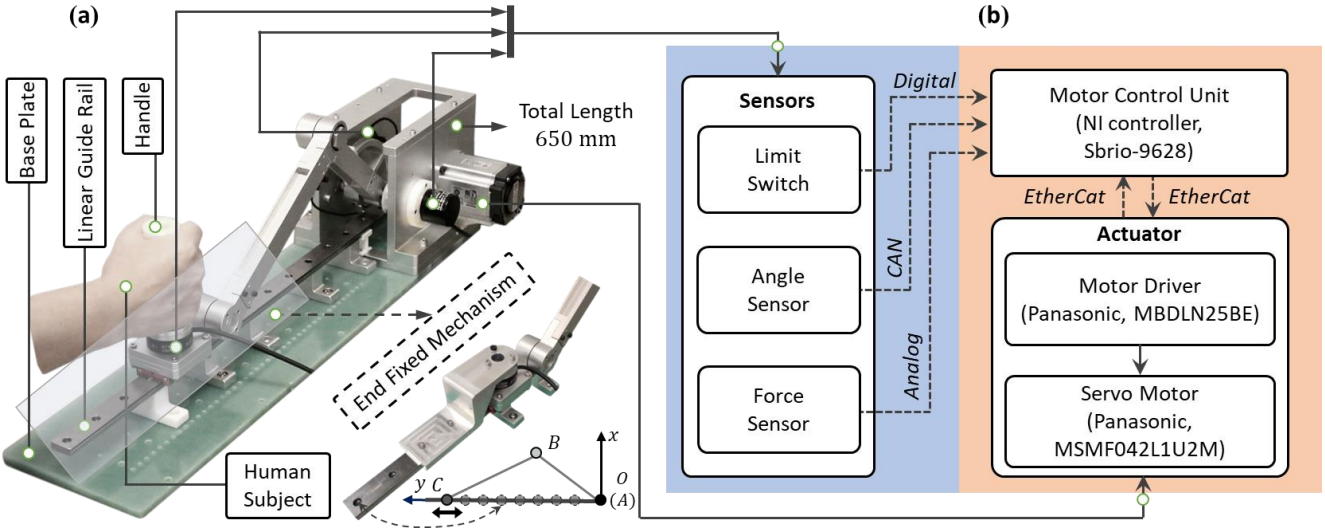

Fig. 4. (a) Prototype of the single-DOF haptic robot. (b) Electronic implementation of the system.

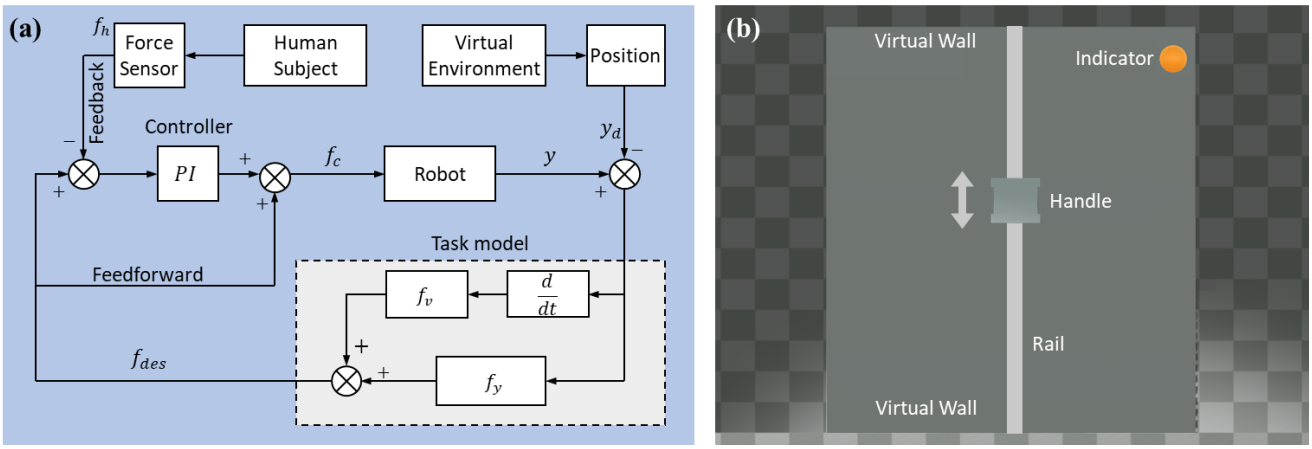

Fig. 5. (a) Diagram of the control block with closed-loop impedance control. (b) Virtual environment for the rendering of free motion and hard contact.

Fig. 4 (b) presents the electronic implementation of the system. An absolute encoder with CAN protocol (resolution: 15 bits, OidE, China) connected with the driven wheel is used to obtain the kinematic parameters of the active joint. The robot is sensorized with a six-axis force sensor (Sunrise Instruments, M3703B2, China). Moreover, two limit switches with digital output are included in the robot to limit the rotation angle of the driven wheel. To perform a high-quality single-DOF motion, the motor driver is connected to the master real-time NI over EtherCAT. The control is realized with LabVIEW 2020 using the LabVIEW FPGA Module to read the signal of digital input, analog input, and CAN input.

B. Robot Control

The closed-loop impedance control is utilized to obtain a high-quality haptic rendering [20, 32, 33] due to its advantages of smaller impedance error caused by the dynamics of the haptic device. Fig. 5 (a) presents the control block with closed-loop impedance control, where the proportional-integral (PI) control with a feedforward term is used to track the desired force. The desired force f_{des} is generated based on the task model that is generally defined as functions of the end position (f_y) and end velocity (f_v). In this work, f_{des} was defined by a virtual wall model.

$$f_{des} = k_n(y - y_d) + b_n v \tag{10}$$

where k_n is the virtual stiffness, b_n is the virtual damping, y and y_d are the position of the handle and virtual wall, respectively, v is the velocity of the handle.

IV. Experiments

This section aims to verify the robot performance in terms of workspace, force feedback capacity, and task rendering capacity. Detailed experimental procedures are also presented in the accompanying video. The study was approved by the Southern University of Science and Technology, Human Participants Ethics Committee (20190004) and consents were obtained from the participant.

A. Workspace and Force Feedback Capacity

Test of workspace: The human subject (male, age 33 years, height 1.78 m, weight 70.5 kg) was required to grasp the

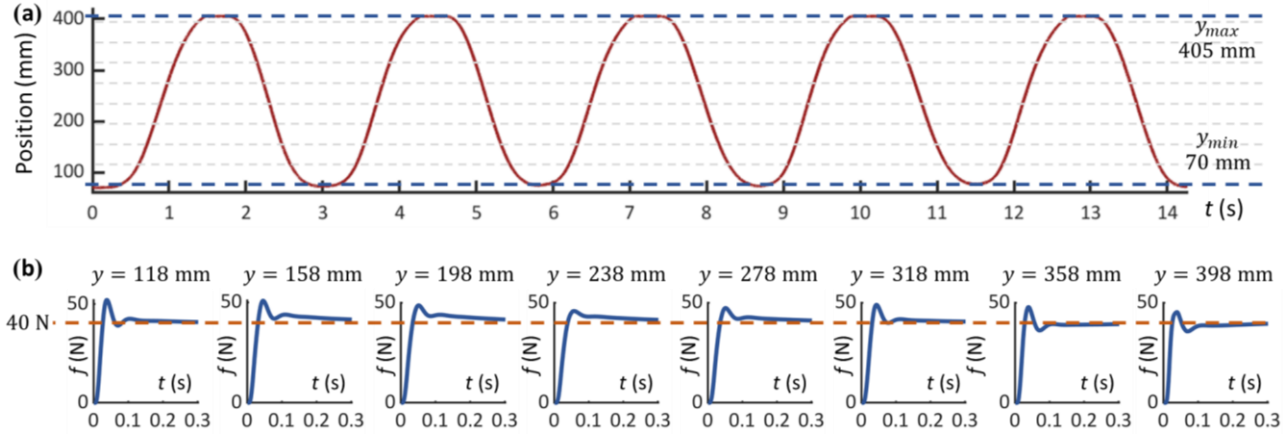

Fig. 6. (a) Moving trajectory of the handle in the workspace. (b) The force step response of the haptic robot at eight different positions.

handle as shown in Fig. 4 (a) in a seated position. Then the human subject moved the handle along the linear guide rail with the position data recorded.

Force feedback capacity: For this non-Cartesian haptic robot, its mechanical properties are not uniform within the workspace, and thus different force feedback capacity could arise at different test points. To this end, we designed a fixed mechanism as shown in Fig. 4 (a). It can fix the endpoint at different positions. Considering the distribution of mounting holes on the guide rail, eight points with y-coordinates of 118 mm, 158 mm, 198 mm, 238 mm, 278 mm, 318 mm, 358 mm, and 398 mm were selected. The step signal from a baseline force of 0 N to a target force of 40 N was commanded to the robot at each position. The force response data were recorded through the six-axis force sensor.

B. Task Rendering Capacity

Free motion and hard contact were two representative interaction tasks. Test of the task rendering capacity of the haptic robot was verified by rendering these two tasks. In the following tests, the participant was required to grasp the handle and interact with the virtual task through the developed robot as shown in Fig. 4 (a). A virtual interface, as illustrated in Fig. 5 (b), was built using Unity 3D (Unity Technologies, San Francisco, CA, US) game engine. The top and bottom borders were set as virtual walls. Position of the wall can be reset by changing the border value.

Free motion rendering capacity: The interactive force is virtually zero in this test. Thus, corresponding desired force f_{des} was set as zero, i.e., setting the variables in (10) as $k_n = 0$, $b_n = 0$. We adopted various control parameters in different motion directions to reduce the impact of the links' gravity. Let the human participant move the handle along a linear reciprocating trajectory. Then the velocity and the resistance force can be measured by sensors.

Hard contact rendering capacity: High stiffness performance is necessary for hard contact rendering. We verified the hard contact rendering capacity by testing the stiffness output performance of the robot. The virtual wall model defined in (10) was used to test the stiffness performance of the system. Variable $k_n = 40\ \mathrm{N \cdot mm^{-1}}$ was

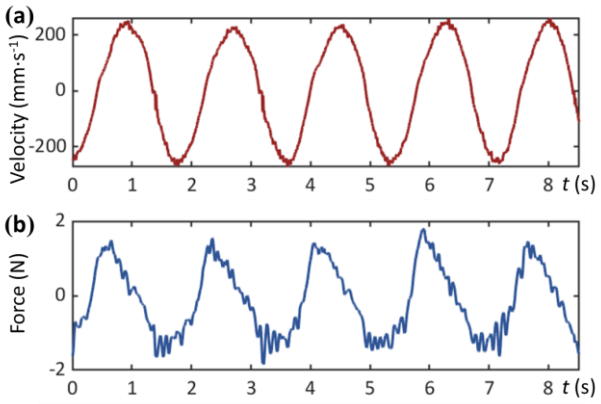

Fig. 7. Free motion test results of (a) end velocity and (b) resistant force.

defined as the stiffness of the virtual wall. Since an appropriate damping coefficient can improve the stiffness property effectively [34], we set the variable b_n in (10) as $0.06\ \mathrm{N \cdot mm^{-1} \cdot s}$. The stiffness performance of the eight different positions was tested to verify whether the robot can achieve high stiffness output throughout the workspace. During the test, the human participant was required to move the handle to the position of the virtual wall first, and then gradually increased the force applied to the wall. When the force reached above 20 N, the human participant can relax the handle. Force and displacement data were recorded.

V. Results and Discussion

Fig. 6 (a) shows the movement trajectory of the endpoint when the operator moves the handle in the workspace. The minimum value of $y-$coordinates is 70 mm (y_{min}) and the maximum is 405 mm (y_{max}). The range of motion is larger than the expected workspace (300 mm). The force step response curves of the eight different positions in the workspace are shown in Fig. 6 (b). The results show that the robot can output the force of 40 N at each position with a fast response that the step rise time is 16.6 ± 3.5 ms (mean±SD). Therefore, the optimized haptic robot meets the design requirements in terms of workspace and force output performance.

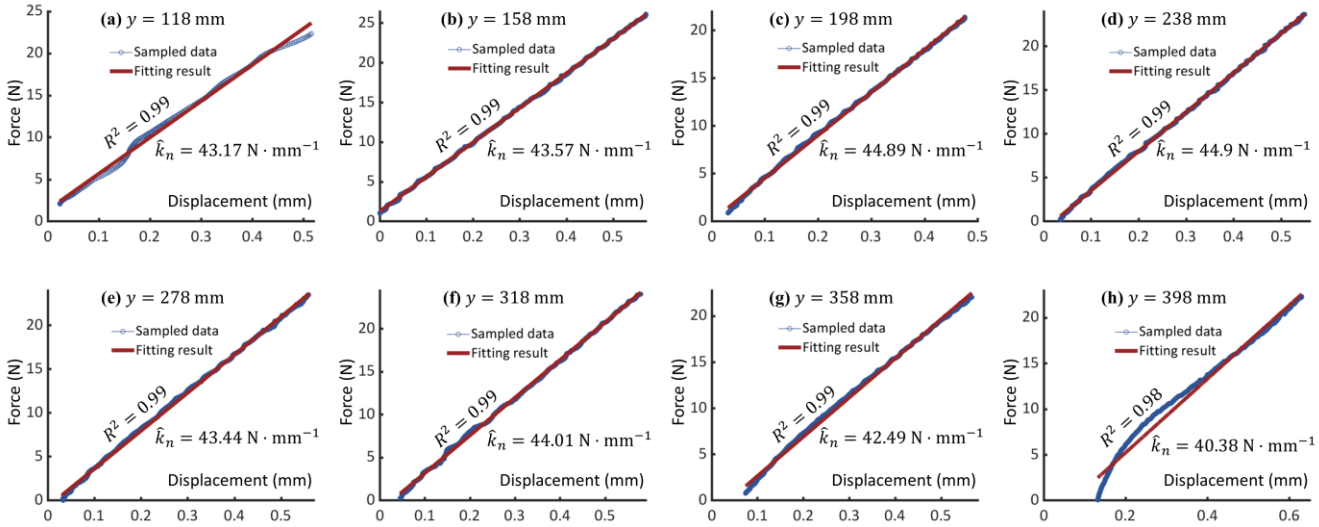

Fig. 8. Stiffness test results at eight different positions in the workspace. The given virtual wall model is $k_n = 40$ N · mm^{-1}, $b_n = 0.06$ N · mm^{-1} · s.

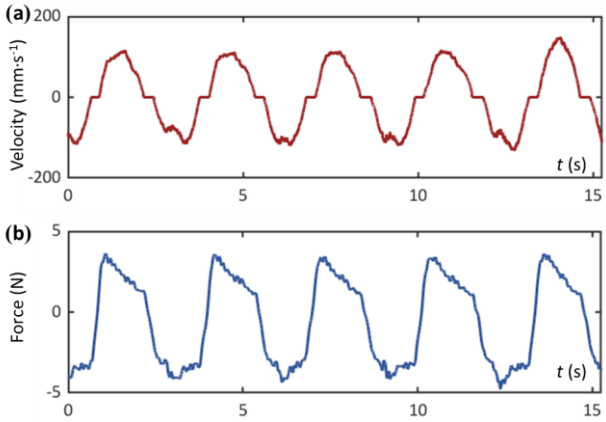

Fig. 9. The resistant force of the back-drivability test when the motor is disabled.

Results of the free motion test are displayed in Fig. 7. As shown in Fig. 7 (a), the human participant moved the handle with the velocity amplitude of 250 mm · s^{-1} and the frequency of 1.5 Hz. It can be obtained from Fig. 7 (b) that the perceived resistance is very little, and the root mean square (RMS) of the resistant force is only 0.93 N. It demonstrates that the developed haptic robot can perform free motion tasks.

Figs. 8 (a)~(h) show the sample force-displacement curves at eight different positions of the virtual wall. The measured stiffness $\hat{k}_n$ is estimated by the slope of the fitting line. It is noted that several fitting lines do not have zero intersects, which may be caused by the links' gravity, but this has a negligible impact on the test results. It can be obtained that the robot can render the stiffness of 40 N · mm^{-1} at all test positions. The curve at $y = 398$ mm is not as linear as the other positions which may be due to the high transmission angle near the edge of the workspace. Previous research suggested that stiffness higher than 24.2 N · mm^{-1} is required to convey hard contact [35]. Thus, the developed robot in this work has the ability to render hard contact.

Compared with other transmissions (e.g., gearbox, ballscrew, and belt), the developed cable-driven robot also has some defects. The linkage design is not easily compatible. The friction force produced by the force perpendicular to the rail affects the back-drivability of the robot. We overcome the above shortcomings through low gear ratio design and optimization process. The device is only 650 mm in length enabling the robot with portability, which makes it comparable to other devices. To test the back-drivability, the handle was moved by the operator with a velocity of 100 mm · s^{-1}, where the device was actuated only by the human participant (without motor compensation). As shown in Fig. 9, the mean resistant force was only 2.5 N. It demonstrates that the robot can be easily back-driven even when the motor is disabled in an accident situation, ensuring interaction safety.

VI. Conclusion

This paper presented our efforts to optimize and develop a single-DOF cable-driven haptic robot with an appropriate tradeoff for workspace and portability, as well as for low gear ratio and force rendering capacity. Using a multi-objective optimization method, we confirmed the design requirements outlined in the introduction. First, we optimized for a compact size that meets the constraint of a given workspace, allowing for appropriate workspace and portability. Second, we optimized for low inertia, high back-drivability, and high force output while meeting the constraints of a low gear ratio of 12:1 and an output force of 40 N. Based on the optimization results, we developed a slider-crank-mechanism-based cable-driven haptic robot capable of free motion and hard contact. Performance evaluations confirmed that the robot meets design requirements for workspace and force rendering capacity. Future work will focus on exploring the robot's ability to perform more realistic tasks and investigate its clinical efficacy.

REFERENCES

[1] N. A. Bayona, J. Bitensky, K. Salter, and R. Teasell, "The role of task-specific training in rehabilitation therapies," *Top. Stroke Rehabil.,* vol. 12, no. 3, pp. 58-65, 2005.

[2] I. J. Hubbard, M. W. Parsons, C. Neilson, and L. M. Carey, "Task-specific training: evidence for and translation to clinical practice," *Occup. Ther. Int.,* vol. 16, no. 3-4, pp. 175-89, 2009.

[3] H. I. Krebs, N. Hogan, M. L. Aisen, and B. T. Volpe, "Robot-aided neurorehabilitation," *IEEE Trans. Rehabil. Eng.,* vol. 6, no. 1, pp. 75-87, 1998.

[4] C. Faure *et al.*, "Adding haptic feedback to virtual environments with a cable-driven robot improves upper limb spatio-temporal parameters during a manual handling task," *IEEE Trans. Neural Syst. Rehabil. Eng.,* vol. 28, no. 10, pp. 2246-2254, 2020.

[5] A. Otaran, O. Tokatli, and V. Patoglu, "Physical Human-Robot Interaction Using HandsOn-SEA: An Educational Robotic Platform With Series Elastic Actuation," *IEEE Trans. Haptics,* vol. 14, no. 4, pp. 922-929, 2021.

[6] Ö. Özen, K. A. Buetler, and L. Marchal-Crespo, "Towards functional robotic training: motor learning of dynamic tasks is enhanced by haptic rendering but hampered by arm weight support," *J. NeuroEng. Rehabil.,* vol. 19, no. 1, p. 19, 2022.

[7] J. Arata, N. Ikedo, and H. Fujimoto, "New multi-d.o.f. haptic device using a parallel mechanism with a wide rotational working area," *Adv. Robot.,* vol. 26, no. 1-2, pp. 121-135, 2012.

[8] P. Lambert and J. L. Herder, "A 7-DOF redundantly actuated parallel haptic device combining 6-DOF manipulation and 1-DOF grasping," *Mech. Mach. Theory,* vol. 134, pp. 349-364, 2019.

[9] S. Lee and S. Kim, "Analysis and optimal design of a new 6 DOF parallel type haptic device," in *Proc. IEEE/RSJ Int. Conf. Intell. Robots Syst.*, 2006, pp. 460-465.

[10] P. Maciejasz, J. Eschweiler, K. Gerlach-Hahn, A. Jansen-Troy, and S. Leonhardt, "A survey on robotic devices for upper limb rehabilitation," *J. NeuroEng. Rehabil.,* vol. 11, Jan 9 2014, Art no. 3.

[11] S. Khalid, F. Alnajjar, M. Gochoo, A. Renawi, and S. Shimoda, "Robotic assistive and rehabilitation devices leading to motor recovery in upper limb: a systematic review," *Disabil. Rehabil.-Assist. Technol.,* pp. 1-15, 2021.

[12] D. J. Reinkensmeyer, L. E. Kahn, M. Averbuch, A. McKenna-Cole, B. D. Schmit, and W. Z. Rymer, "Understanding and treating arm movement impairment after chronic brain injury: progress with the ARM guide," *J. Rehabil. Res. Dev.,* vol. 37, no. 6, pp. 653-62, 2000.

[13] R. Colombo *et al.*, "Design strategies to improve patient motivation during robot-aided rehabilitation," *J. NeuroEng. Rehabil.,* vol. 4, p. 3, 2007.

[14] J. J. Chang, W. L. Tung, W. L. Wu, M. H. Huang, and F. C. Su, "Effects of robot-aided bilateral force-induced isokinetic arm training combined with conventional rehabilitation on arm motor function in patients with chronic stroke," (in eng), *Arch. Phys. Med. Rehabil.,* vol. 88, no. 10, pp. 1332-8, Oct 2007.

[15] Y.-f. Lu, D.-p. Fan, H. Liu, and M. Hei, "Transmission capability of precise cable drive including bending rigidity," *Mech. Mach. Theory,* vol. 94, pp. 132-140, 2015.

[16] Y. Mao and S. K. Agrawal, "Design of a Cable-Driven Arm Exoskeleton (CAREX) for Neural Rehabilitation," *IEEE Trans. Robot.,* vol. 28, no. 4, pp. 922-931, 2012.

[17] R. Chu, Y. Zhang, H. Zhang, W. Xu, J. H. Ryu, and D. Wang, "Co-Actuation: A Method for Achieving High Stiffness and Low Inertia for Haptic Devices," *IEEE Trans. Haptics,* vol. 13, no. 2, pp. 312-324, 2020.

[18] Y. J. Kim, "Anthropomorphic Low-Inertia High-Stiffness Manipulator for High-Speed Safe Interaction," *IEEE Trans. Robot.,* vol. 33, no. 6, pp. 1358-1374, 2017.

[19] P. Liang, H. Zeng-Guang, P. Long, and W. Weiqun, "Design of CASIA-ARM: A novel rehabilitation robot for upper limbs," in *Proc. IEEE/RSJ Int. Conf. Intell. Robots Syst.*, 2015, pp. 5611-5616.

[20] J. Arata, H. Kondo, N. Ikedo, and H. Fujimoto, "Haptic device using a newly developed redundant parallel mechanism," *IEEE Trans. Robot.,* vol. 27, no. 2, pp. 201-214, 2011.

[21] M. Vulliez, S. Zeghloul, and O. Khatib, "Design strategy and issues of the Delthaptic, a new 6-DOF parallel haptic device," *Mech. Mach. Theory,* vol. 128, pp. 395-411, 2018.

[22] E. P. Washabaugh, J. Guo, C. K. Chang, C. D. Remy, and C. Krishnan, "A Portable Passive Rehabilitation Robot for Upper-Extremity Functional Resistance Training," *IEEE Trans. Biomed. Eng.,* vol. 66, no. 2, pp. 496-508, 2019.

[23] J.-A. Leal-Naranjo, J.-A. Soria-Alcaraz, C.-R. Torres-San Miguel, J.-C. Paredes-Rojas, A. Espinal, and H. Rostro-González, "Comparison of metaheuristic optimization algorithms for dimensional synthesis of a spherical parallel manipulator," *Mech. Mach. Theory,* vol. 140, pp. 586-600, 2019.

[24] A. M. Oosterwijk, M. K. Nieuwenhuis, C. P. van der Schans, and L. J. Mouton, "Shoulder and elbow range of motion for the performance of activities of daily living: A systematic review," *Physiother. Theory Pract.,* vol. 34, no. 7, pp. 505-528, 2018.

[25] C. F. Yeong, A. Melendez-Calderon, and E. Burdet, "Analysis of pick-and-place, eating and drinking movements for the workspace definition of simple robotic devices," in *Proc. Int. Conf. Rehabil. Robot.*, 2009, pp. 46-52.

[26] L. Yin and K. Annett-Hitchcock, "Comparison of body measurements between Chinese and U.S. females," *J. Text. Inst.,* vol. 110, no. 12, pp. 1716-1724, 2019.

[27] Y. J. Wang, P. Y. Mok, Y. Li, and Y. L. Kwok, "Body measurements of Chinese males in dynamic postures and application," *Appl. Ergon.,* vol. 42, no. 6, pp. 900-912, 2011.

[28] A. Molaei, N. A. Foomany, M. Parsapour, and J. Dargahi, "A portable low-cost 3D-printed wrist rehabilitation robot: Design and development," *Mech. Mach. Theory,* vol. 171, p. 104719, 2022.

[29] K. Oh, W. Z. Rymer, I. Plenzio, F. A. Mussa-Ivaldi, S. Park, and J. Choi, "Development of a Planar Haptic Robot With Minimized Impedance," *IEEE Trans. Biomed. Eng.,* vol. 68, no. 5, pp. 1441-1449, 2021.

[30] C. Gosselin and J. Angeles, "A global performance index for the kinematic optimization of robotic manipulators," *J. Mech. Des.,* vol. 113, no. 3, pp. 220-226, 1991.

[31] K. Deb, A. Pratap, S. Agarwal, and T. Meyarivan, "A fast and elitist multiobjective genetic algorithm: NSGA-II," *IEEE Trans. Evol. Comput.,* vol. 6, no. 2, pp. 182-197, 2002.

[32] A. Q. L. Keemink, H. van der Kooij, and A. H. A. Stienen, "Admittance control for physical human–robot interaction," *Int. J. Robot. Res.,* vol. 37, no. 11, pp. 1421-1444, 2018.

[33] C. R. Carignan and K. R. Cleary, "Closed-loop force control for haptic simulation of virtual environments," 2000.

[34] F. E. v. Beek, D. J. F. Heck, H. Nijmeijer, W. M. B. Tiest, and A. M. L. Kappers, "The Effect of Global and Local Damping on the Perception of Hardness," *IEEE Trans. Haptics,* vol. 9, no. 3, pp. 409-420, 2016.

[35] H. Z. Tan, M. A. Srinivasan, B. Eberman, and B. Cheng, "Human factors for the design of force-reflecting haptic interfaces," *Dynamic Systems and Control,* vol. 55, no. 1, pp. 353-359, 1994.